THE JOURNAL OF PHYSICAL CHEMISTRY C
A JOURNAL OF THE AMERICAN CHEMICAL SOCIETY

pubs.acs.org/JPCC Article

Enhancing Catalytic Properties of Iron- and Nitrogen-Doped Carbon for Nitrogen Reduction through Structural Distortion: A Density Functional Theory Study

Weitao Shan and Guofeng Wang*

Cite This: *J. Phys. Chem. C* 2021, 125, 16004−16012 Read Online

ABSTRACT: In this study, we have performed the first-principles density functional theory calculations to predict the influence of structural distortion on the catalytic properties of Fe, N codoped carbon (Fe−N−C) for the nitrogen reduction reaction (NRR). On both FeN_4 and FeN_3 sites embedded in a graphene layer, our results show that compressive strain not only enhances the NRR activity manifested by a positive change in NRR limiting potential, but also changes the favorable NRR pathway from a hybrid path to a distal one. The activity enhancement is attributed to the strong binding of NRR intermediate species, *NNH, on the strained active sites. Moreover, we predict that the NRR selectivity on both FeN_4 and FeN_3 sites is improved by the structural distortion induced by compressive strain. Hence, our computational results suggest that the degree of compressive strain in the graphene layer of Fe−N−C catalysts could be tuned to enhance their catalytic activity and selectivity for NRR.

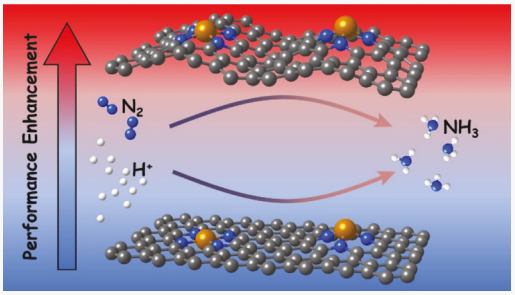

1. INTRODUCTION

As one of the most important chemicals in agricultural industries, ammonia (NH_3) plays a fundamental role in producing fertilizers to support large population in the world.[1,2] Ammonia is also a great clean energy resource as it stores 17.6% hydrogen by mass with no CO_2 emission.[3] The Haber-Bosch process is widely used to produce ammonia on an industrial scale. However, the Haber-Bosch process has an intensive requirement of H_2, whose production consumes nearly 1−2% of the global annual energy generation and emits 300 metric tons of CO_2 every year.[2−5]

The electrochemical conversion is acknowledged as a sustainable and economic alternative method to the Haber-Bosch method for nitrogen reduction reaction (NRR) to produce ammonia under ambient conditions.[6−8] The development of electrocatalysts for NRR focuses on addressing the issues related to low activity due to the large overpotential of NRR, and low selectivity because of the competing hydrogen evolution reaction (HER).[2,9−12] Much progress has been made in improving the catalytic performance of NRR on the surface of metal catalysts, such as Ru,[13−15] Pt,[16,17] Au,[18−20] Ni,[21,22] and Mo.[23] However, the large overpotential for N_2 activation and limited NH_3 selectivity are inevitable barriers for the application of metal catalysts.[10,11,24,25] Non-noble metal oxides, chalcogenides, borides, and carbides (NiO, ZnS, NiS, CdS, TiB_2 etc.) were also studied, and the chalcogenides and borides were identified as potential NRR electrocatalysts under ambient conditions.[26−29]

As a promising candidate of NRR electrocatalysts, the metal and nitrogen codoped carbon has exhibited some technical advantages such as the prevailing NRR performance, high conductivity after doping, and mechanical flexibility when deposited onto the electrode.[11,12] Tian et al. theoretically predicted Mo, N codoped graphene to be a potential NRR catalyst, in which the Mo−N moiety acted as the active site for N_2 bond breaking, and the graphene worked as an electron transmitter and reservoir.[30] A computational study by Jung et al. has shown such a kind of catalysts with single metal atom embedded in N-doped graphene has better NRR selectivity than metal catalysts, and some cases (i.e., TiN_4 and VN_4) even have better activity than Ru due to a strong bonding between the central metal atom and adsorbed N_2.[31] Our previous study on Ni−N−C catalysts for NRR showed a high faradaic efficiency (FE) of 21 ± 1.9%, and a NH_3 production rate of 115 $\mu g \cdot h^{-1} \cdot cm^{-2}$ under ambient conditions.[32] Recently, the studies on catalysts with a single Ru atom embedded on N-doped graphene have, respectively, shown greatly promoted NH_3 yield rates of 0.121 $mg_{NH_3} \cdot mg_{cat.}^{-1} \cdot h^{-1}$[33] and 3.665 $mg_{NH_3} \cdot$

Received: May 22, 2021
Revised: July 3, 2021
Published: July 21, 2021

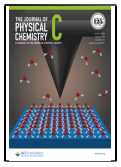

https://doi.org/10.1021/acs.jpcc.1c04510
J. Phys. Chem. C 2021, 125, 16004−16012

$mg_{Ru}^{-1}\cdot h^{-1}$,[34] which are promising and these types of catalysts have a good opportunity for future NRR applications.

As a crustal abundant element, Fe was already found to combine with Mo to form a FeMo cofactor in the nitrogenase, which is a key component for natural N_2 fixation.[35,36] In an early NRR electrochemical study, Fe-phthalocyanine catalysts showed a FE of 0.33% and a NH_3 production rate of 5.57×10^{-10} $mol\cdot s^{-1}\cdot cm^{-2}$.[37] A Fe-doped metal−organic framework catalyst was synthesized by Chen et al. using a hydrothermal method, whose NH_3 production rate and current efficiency could, respectively, reach 2.12×10^{-9} $mol\cdot s^{-1}\cdot cm^{-2}$ and 1.43% under 90 °C.[38] A very recent study on the tetraphenylporphyrin iron chloride (FeTPPCl) showed a promising NRR activity with a FE of 16.76 ± 0.9% and a NH_3 production rate of 18.28 ± 1.6 $\mu g\cdot h^{-1}\cdot mg_{cat.}^{-1}$ in neutral electrolytes.[39] Zhang et al. reported a highly active iron porphyrin-based catalyst (Fe−TCPP) with a 44.77 $\mu g\cdot h^{-1}\cdot mg_{cat.}^{-1}$ NH_3 production rate and a 16.23% FE.[40] Rationally designed and synthesized single iron and N,O-doped carbon (Fe−NO−C) catalysts were studied by Hou et al.[41] Their catalysts reached a high NH_3 production rate of 31.9 $\mu g\cdot h^{-1}\cdot mg_{cat.}^{-1}$ and a FE of 11.8%. A Fe, N codoped carbon nanotube catalyst with active FeN_3 sites was designed by Zheng et al. as an enhanced NRR catalyst.[42] It exhibited encouraging NRR catalytic performance with a NH_3 production rate of 34.83 $\mu g\cdot h^{-1}\cdot mg_{cat.}^{-1}$ and a FE of 9.28%. A study by Lü et al. reported a single Fe and N codoped site NRR catalyst that was synthesized from the ZIF-8 precursor, which has a high FE of 18.6 ± 0.8% and a NH_3 yield rate of 62.9 ± 2.7 $\mu g\cdot h^{-1}\cdot mg_{cat.}^{-1}$.[43]

It should be noted that high-temperature treatment is an essential step during the synthesis of metal and nitrogen codoped carbon catalysts in the aforementioned studies.[32,34,42,43] As already elaborated in previous studies on graphene membranes, a negative thermal expansion coefficient of graphene would result in a wrinkle configuration at elevated temperature.[44−47] However, to the best of our knowledge, all the previous theoretical studies on Fe−N−C catalysts only assumed the FeN_x active sites embedded in a fully relaxed planar graphene layer. Our previous studies on the oxygen reduction reaction (ORR) and carbon dioxide reduction reaction (CO2RR) on Fe−N−C catalysts have demonstrated that the compressive strain caused by the elevated-temperature treatment has a beneficial effect in facilitating their catalytic activity.[48,49] Herein, we employed the first-principles density functional theory (DFT) to study how the compressive strain in graphene layers would affect the NRR activity and selectivity on both FeN_4 and FeN_3 sites embedded in the graphene layer. Our results suggest that structural distortion could be used to enhance the catalytic properties of metal and nitrogen codoped carbon catalysts for NRR.

2. COMPUTATIONAL METHODS

The spin-polarized DFT[50−52] calculations were performed using the Vienna Ab Initio Simulation package (VASP).[53−56] The projector augmented wave[57] pseudopotential was employed in conjunction with the Perdew−Burke−Ernzerhof[58] generalized gradient approximation.[59] The van der Waals correction was included using the Tkatchenko−Scheffler method.[60,61] A plane wave basis set with a kinetic energy cutoff of 400 eV was used to expand the wave functions. The energy convergence was set to be 1×10^{-6} eV and the atomic structures were relaxed to the tolerance of atomic force below 0.01 eV/Å. As shown in Figure 1a, a FeN_4 site was modeled in a 9.84 × 8.52 Å periodic supercell of a graphene layer by replacing six C atoms with a central Fe atom and four surrounding pyridinic N atoms. A FeN_3 site model (Figure 1b) was modeled in the same supercell of a graphene layer by replacing four C atoms with a central Fe atom and three surrounding pyridinic N atoms. A 14 Å vacuum space was added perpendicular to the graphene layer to minimize interaction between periodic images. The Brillouin zone was sampled by a 4 × 4 × 1 Monkhorst−Pack grid[62] for both FeN_4 and FeN_3 models.

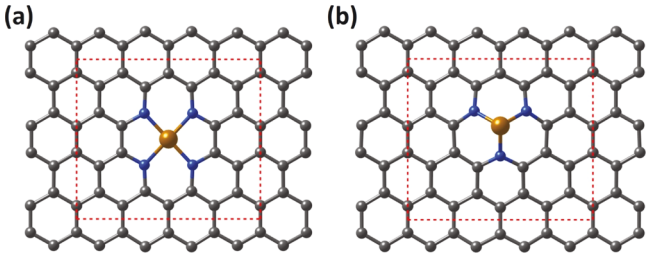

Figure 1. Atomic structures of (a) FeN_4 and (b) FeN_3 sites in a graphene layer shown from a top view. The periodic unit cells of these two active site models are marked with the red rectangles. In the figure, the gray, blue, and golden balls represent C, N, and Fe atoms, respectively.

The free energy of the adsorbed intermediates was calculated using the reversible hydrogen electrode (RHE) as the reference, for which the free energy of a pair of proton and electron ($H^+ + e^-$) is calculated as the free energy of 1/2 H_2.[24,63] The free energy change ΔG of any chemical species can be calculated as

$$\Delta G = \Delta E_{ads} + \Delta E_{ZPE} - T\Delta S - \Delta G_U$$

where ΔE_{ads} denotes the adsorption energy of the chemical species on active site and ΔE_{ZPE} represents the zero-point energy correction. The zero-point energy for each species was calculated by the summation of each vibrational mode of binding molecules and adatoms as $\sum \frac{1}{2} h\nu_i$, where ν_i is the ith vibrational frequency. The entropy change ΔS from the vibrational contribution of adsorbates at room temperature was evaluated in the harmonic vibrational mode. The entropy change of free molecules under standard conditions was taken from the NIST database.[64] The energy shift from applied electrode potential U was evaluated as $\Delta G_U = neU$, where n is the number of electrons transferred in the reaction and the electrode potential U is given with the reference to the RHE. The crystal orbital Hamilton population (COHP) analysis was carried out using program LOBSTER.[65−68]

3. RESULTS AND DISCUSSION

3.1. Atomic Models of NRR Active Sites with Structural Distortion. It has been reported that both FeN_4[31,43,69] and FeN_3[42,70] moieties embedded in a graphene layer exhibit activity for NRR. Consequently, in the present study, we focused on the effect of structural distortion on the FeN_4 and FeN_3 sites. The FeN_4 site consists of a central Fe atom at a double-vacancy site and four neighboring pyridinic N atoms (Figure 1a). The FeN_3 site consists of a central Fe atom at a single-vacancy site and three adjacent pyridinic N atoms (Figure 1b). As revealed in a previous study,[45] layered graphene could experience a biaxial compression and form wrinkles after a high-temperature treatment. A wrinkle

https://doi.org/10.1021/acs.jpcc.1c04510
J. Phys. Chem. C 2021, 125, 16004−16012

configuration of the FeN_4 site was found to kinetically improve the activity for ORR, and thermodynamically promote the activity for CO2RR on Fe−N−C catalysts.[48,49] Motivated by these previous results, we herein computationally examined the effect of compressive strain on the activity and selectivity on FeN_4 and FeN_3 sites for NRR.

The atomic models of FeN_4 and FeN_3 sites with compressive strain are shown in Figure 2. For comparison,

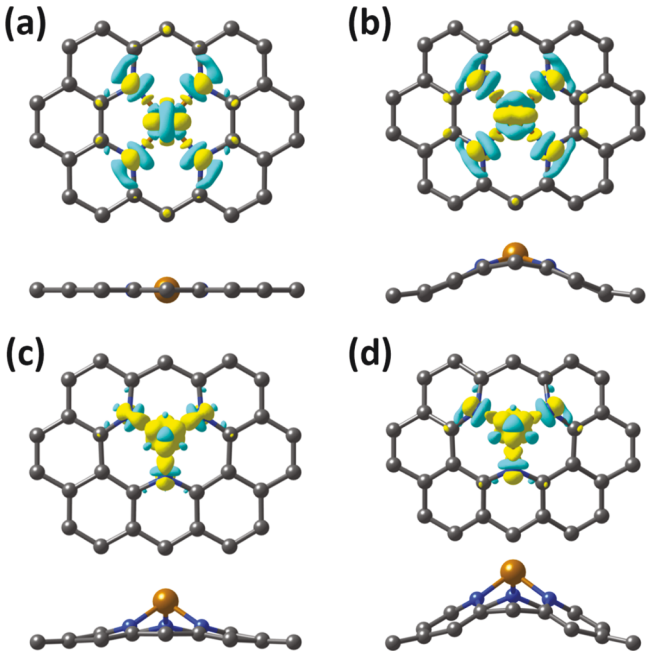

Figure 2. Computed charge distribution and the corresponding atomic side view of (a) unstrained FeN_4, (b) strained FeN_4, (c) unstrained FeN_3, and (d) strained FeN_3 sites. The charge accumulation and depletion on each active site are shown, respectively, by the yellow and cyan clouds with an isosurface of 0.0075 e/Å^3. In the figure, the gray, blue, and golden balls represent C, N, and Fe atoms, respectively.

each active site was modeled in a fully relaxed state (i.e., unstrained) and in a compressively strained state. In the unstrained FeN_4 site (Figure 2a), the Fe atom lies in the planar graphene layer after structural optimization. In contrast, the Fe atom in the unstrained FeN_3 site (Figure 2c) is predicted to be out of the graphene layer by 0.32 Å. The compressively strained FeN_4 and FeN_3 site models were constructed by contracting the graphene layer to the same degree and making them have a similarly curved layer. The compressive strain turns the initial planar graphene layer into a wrinkle configuration as shown in Figure 2b,d. The wrinkles containing the strained FeN_4 and FeN_3 sites are found to have a height of 1.27 and 1.29 Å, respectively. The central Fe atom is displaced out of the graphene layer by 0.28 and 1.48 Å in the strained FeN_4 and FeN_3 sites, respectively. As a result of compressive strain, the length of the Fe−N bonds is shortened by 2.0 and 0.5% in the strained FeN_4 and FeN_3 sites than that in the corresponding unstrained sites. Moreover, we compared the electronic structures of the FeN_4 (Figure 2a,b) and FeN_3 (Figure 2c,d) sites with and without compressive strain. The charge distributions on the strained FeN_4 sites show that the compressive strain results in a polarized charge distribution on the central Fe atom as the charge accumulation (yellow cloud) and depletion (cyan cloud) are largely separated. In contrast, there is only charge depletion shown on the central Fe atom in the unstrained FeN_4 site model. For FeN_3 sites, the one with compressive strain exhibits more charge depletion separated from the charge accumulation on the Fe atom than that of the unstrained one. In addition, the FeN_3 sites demonstrate a much smaller change in the charge distribution that is caused by the compressive strain than the FeN_4 sites.

3.2. Influence on the NRR Pathway and Activity. Nitrogen reduction is a complex process with many possible intermediate species involved along a reaction pathway. There exist three distinct types of pathways, that is, the distal, alternating, and enzymatic pathways,[6,11,12,71,72] for the electrochemical NRR. The distal and alternating pathways normally start with an end-on adsorption of a N_2 molecule on the catalyst surface, whereas the enzymatic pathway starts with a side-on N_2 adsorption on the catalyst surface. The distal pathway for NRR goes through a reaction sequence in which the distal N of the adsorbed N_2 will be preferably hydrogenated all the way to produce a NH_3 molecule. In contrast, the alternating and enzymatic pathways go through a different reaction sequence in which hydrogenation occurs alternatively on the two N atoms of the adsorbed N_2. To identify the most likely reaction pathway on the modeled FeN_4 and FeN_3 sites, we first used the DFT calculations to predict the most stable adsorption configurations of the NRR intermediate species on the sites. There are nine possible intermediate species (i.e., $*N_2$, *NNH, $*NNH_2$, *NHNH, $*NHNH_2$, $*NH_2NH_2$, *N, *NH, and $*NH_2$) during the reaction of nitrogen reduction. We compared the free energy of all possible adsorption configurations for each intermediate specie to locate the most stable one. Subsequently, the calculated free energy change of each intermediate specie was used to predict the free energy evolution of the competitive NRR pathways.

Our computational results show that the predicted free energy evolution for NRR on the compressively strained FeN_4 site has a much more positive limiting potential than that on the unstrained FeN_4 site (Figure 3a). Here, the limiting potential of NRR ($U_{L(NRR)}$) is defined as the least reverse electrode potential needed to overcome the hydrogenation step with the largest positive free energy change in NRR. Consequently, a more positive $U_{L(NRR)}$ indicates a better NRR activity. Such a hydrogenation step is also called the potential determining step (PDS) in NRR. As shown in Figure 3a, the PDS of NRR on both unstrained and strained FeN_4 sites was found to be the first hydrogenation step from $*N_2$ to *NNH. Our predicted limiting potential for NRR on the unstrained FeN_4 site is −1.31 V (Table 1), which is comparable with a value of −1.36 V from the literature.[69] In addition, our predicted NRR pathway on the unstrained FeN_4 site shares the same PDS as the previous study.[69] As given in Table 1, the compressive strain on the FeN_4 site induces a positive change in $U_{L(NRR)}$ by 0.21 V, which implies that the strained FeN_4 site has better NRR activity than the unstrained one. The compressive strain on the FeN_4 site is also predicted to lead to a change in the NRR pathway (Figure 3b). On the unstrained FeN_4 site, the most favorable NRR pathway was predicted to be a hybrid one. Following this pathway, the NRR starts with the N_2 molecule adsorption in an end-on configuration, and the distal N atom of the adsorbed N_2 is first hydrogenated with two H. Then, the third H is reacted with the proximal N atom of the adsorbed N_2, and the fourth hydrogenation step leads to the dissociation of N−N bond to

https://doi.org/10.1021/acs.jpcc.1c04510
J. Phys. Chem. C 2021, 125, 16004−16012

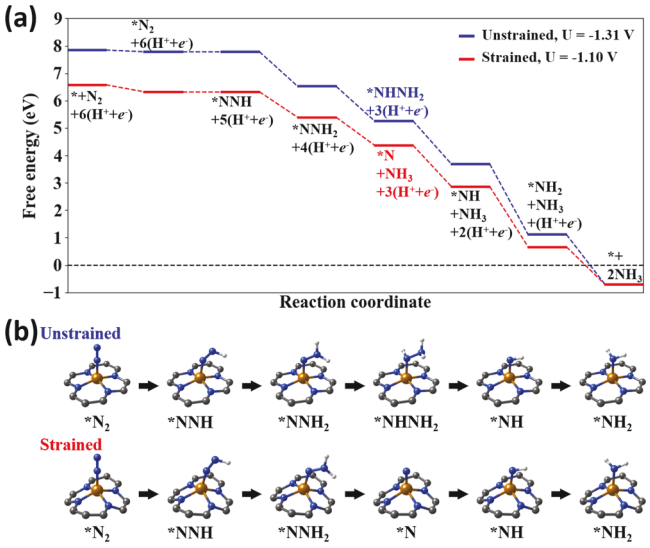

Figure 3. (a) Predicted free energy evolution of the most favorable NRR pathway on the FeN_4 sites with and without compressive strain. The NRR free energy evolution on each active site is shown under its own limiting potential. (b) Atomic structures of the most stable adsorbed species along the favorable NRR pathway on the two FeN_4 sites. The gray, blue, golden, and white balls represent C, N, Fe, and H atoms, respectively.

Table 1. Calculated Limiting Potential of NRR and the Free Energy Change of *NNH Adsorption on FeN_4 and FeN_3 Sites

	FeN_4		FeN_3	
	unstrained	strained	unstrained	strained
$U_{L(NRR)}$ (V)	−1.31	−1.10	−0.83	−0.80
ΔG_{*NNH} (eV)	1.25	0.84	−0.04	−0.13

produce the first NH_3 molecule. Finally, the remained *NH on top of the Fe atom is subsequently hydrogenated until the second NH_3 molecule desorbs from the active site. However, the favorable NRR pathway on the compressively strained FeN_4 site was predicted to be a typical distal pathway. On the strained FeN_4, after the first two hydrogenation steps occur on the distal N atom, the third hydrogenation step is still on the distal N atom of the adsorbed N_2 and leads to the desorption of the first NH_3 molecule produced. Subsequently, the remaining *N atom on the active site is hydrogenated to become the second NH_3 molecule produced.

The predicted free energy evolution of NRR on the unstrained and strained FeN_3 sites is shown in Figure 4a, which also reveals that the first hydrogenation step is the PDS for NRR. As shown in Table 1, $U_{L(NRR)}$ on the unstrained FeN_3 site is predicted to be −0.83 V, which is very close to a previously reported value of −0.84 V.[42] The predicted free energy evolution for NRR on FeN_3 sites indicates that the FeN_3 site with a compressive strain has a slightly better NRR activity than the unstrained one due to a more positive limiting potential of −0.80 V (Table 1). The most favorable NRR pathway on the unstrained FeN_3 site was predicted to be a hybrid one, starting with the N_2 molecule adsorption in an end-on configuration (Figure 4b). In the second hydrogenation step, the adsorption configuration of the most stable intermediate species changes to a side-on *NHNH. Then, one of the N atoms of *NHNH is preferably hydrogenated by two

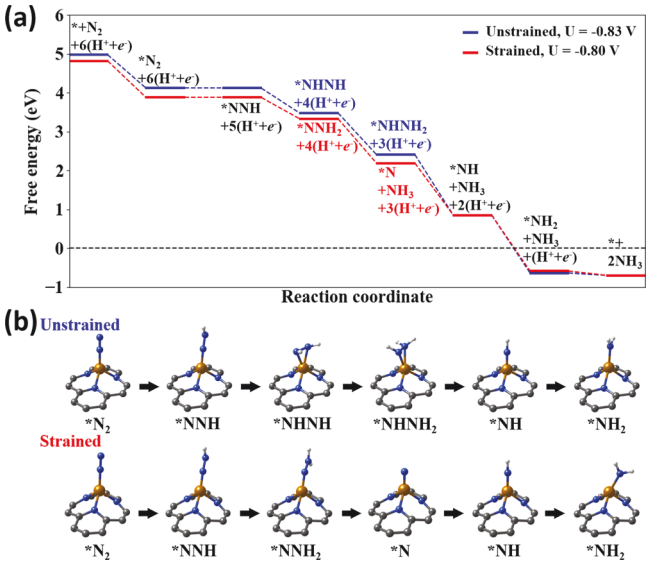

Figure 4. (a) Predicted free energy evolution of the most favorable NRR pathway on the FeN_3 sites with and without compressive strain. The NRR free energy evolution on each active site is shown under its own limiting potential. (b) Atomic structures of the most stable adsorbed species along the favorable NRR pathway on the two FeN_3 sites. The gray, blue, golden, and white balls represent C, N, Fe, and H atoms, respectively.

H to form the first NH_3 molecule, and the remaining *NH is hydrogenated into the second NH_3 molecule produced. With some compressive strain on this FeN_3 site, the NRR pathway was predicted to change to a typical distal one. As shown in Figure 4b, the NRR on the compressively strained FeN_3 site has the same adsorption configurations with the unstrained one in the first two steps, but an end-on $*NNH_2$ adsorption becomes more favored after the second hydrogenation step.

According to our predicted NRR limiting potentials (Table 1), the unstrained FeN_3 site shows a better NRR activity than the unstrained FeN_4 site with a more positive $U_{L(NRR)}$ by 0.48 V, and the strained FeN_3 site also has a more positive $U_{L(NRR)}$ by 0.30 V than the strained FeN_4 site. Thus, it can be inferred that the FeN_3 sites are more active for NRR than the FeN_4 sites in Fe−N−C catalysts. The NRR activity on both FeN_4 and FeN_3 sites is predicted to be enhanced by compressive strain. Moreover, our calculation results in Table 1 demonstrate that compressive strain has an appreciable influence on the NRR activity on FeN_4 sites as the NRR limiting potential has a positive change of 0.21 V due to the structural distortion. In contrast, the NRR limiting potential on the strained FeN_3 site only changes to be more positive by 0.03 V as compared to the unstrained one.

To gain understanding of the compressive strain effect on NRR activity, we have carried out bonding analysis for the adsorption of *NNH on the active sites. It has been pointed out that the intermediate species *NNH is a good descriptor for the NRR activity, as most NRR catalysts hold the step $*N_2 \rightarrow$ *NNH as PDS.[73−76] Indeed, our calculated free energy change for the *NNH adsorption (Table 1) shows a direct correlation with the predicted NRR limiting potential. Namely, the compressively strained sites have lower energy for NNH adsorption and simultaneously exhibit more positive NRR limiting potentials than the corresponding unstrained sites. Specifically, we examined the bonding states between Fe and the proximal N in *NNH using the projected crystal orbital

https://doi.org/10.1021/acs.jpcc.1c04510
J. Phys. Chem. C 2021, 125, 16004−16012

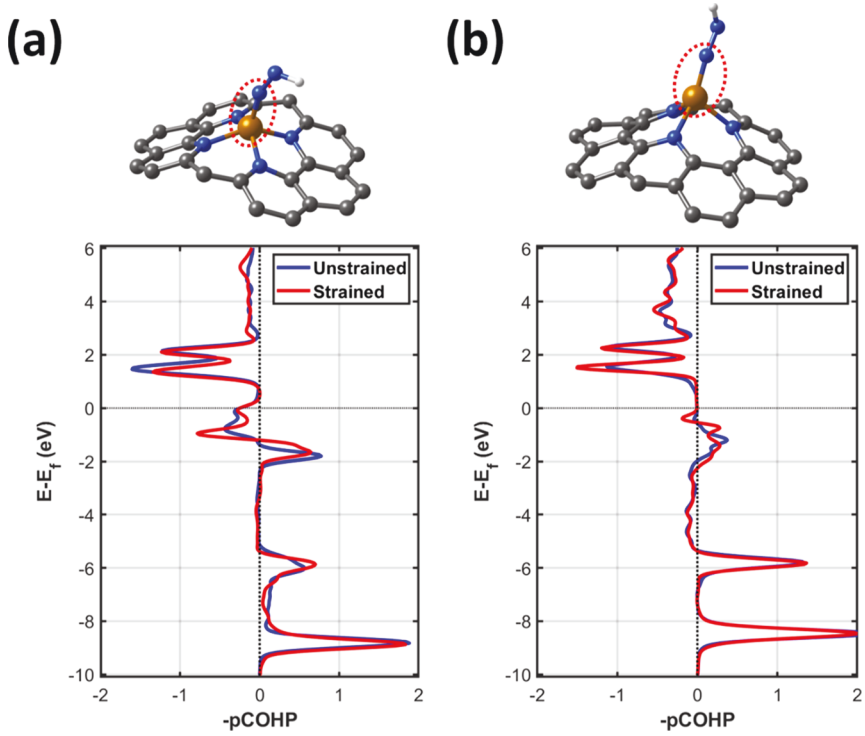

Figure 5. pCOHP analysis for the Fe−N bond between the central Fe and the adsorbed *NNH on (a) FeN_4 and (b) FeN_3 sites with and without strain. The gray, blue, golden, and white balls represent C, N, Fe, and H atoms in the atomic structures, respectively. The Fermi level is set to be 0 eV in the figure.

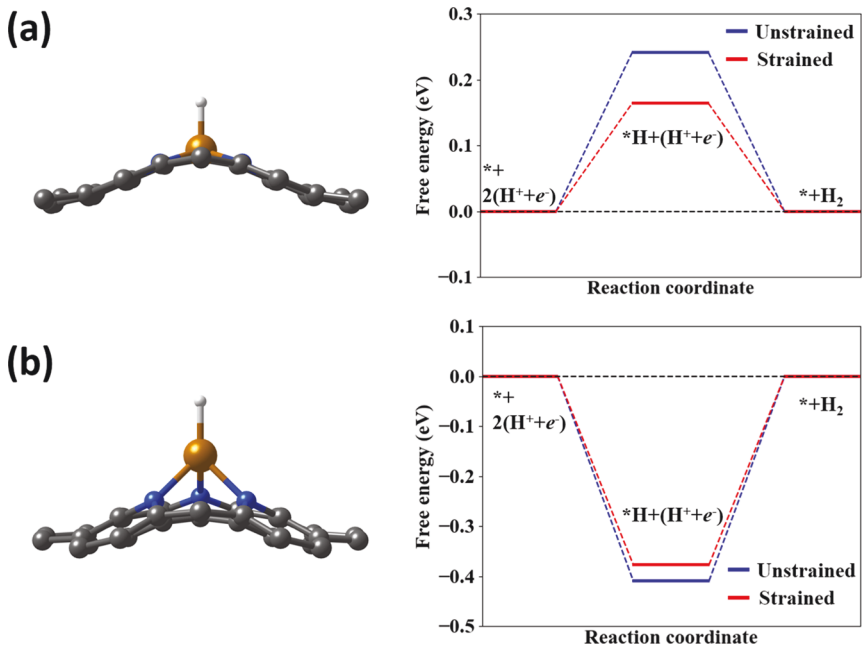

Figure 6. (a) Atomic structure of adsorbed *H on the strained FeN_4 site and calculated free energy evolution for HER on the FeN_4 sites with and without strain. (b) Atomic structure of adsorbed *H on the strained FeN_3 site and calculated free energy evolution for HER on the FeN_3 sites with and without strain. In the figure, the gray, blue, golden, and white balls represent C, N, Fe, and H atoms, respectively.

Hamilton population (pCOHP) analysis[65−68,77] (Figure 5), which was applied in previous NRR catalyst studies.[74,78,79] The bonding and antibonding states of Fe−N are depicted as the positive and negative parts of −pCOHP curves, respectively. Our results show that most of the valence states (i.e., the part below the Fermi level, E_F) are bonding states, whereas a small density of antibonding states exists at the Fermi level for both strained and unstrained FeN_4 sites (Figure 5a). These antibonding states at the Fermi level indicate an unstable bonding between *NNH and Fe, which can also be confirmed by the positive free energy change of *NNH adsorption shown in Table 1. The integrated COHP (ICOHP) up to the Fermi level of the strained FeN_4 site was predicted to be −2.03 eV, which is more negative than that of the unstrained FeN_4 site

https://doi.org/10.1021/acs.jpcc.1c04510
J. Phys. Chem. C 2021, 125, 16004−16012

(−1.96 eV). As revealed in previous studies, a more negative ICOHP indicates a stronger covalent bonding.[74,78,79] Hence, our bond analysis further implies a stronger *NNH binding on the strained FeN_4 site. For unstrained and strained FeN_3 sites, our COHP analysis results show that most valence states appear as bonding, and no states are found at the Fermi level (Figure 5b). In contrast to the results of the FeN_4 site, only a small difference is observed in the −pCOHP curves between the unstrained and strained FeN_3 sites, suggesting a similar bonding strength between Fe and the proximal N of *NNH. Furthermore, the ICOHP of the strained FeN_3 site differs only by 0.01 eV as compared to that of the unstrained FeN_3 site, which also indicates a similar binding strength of *NNH on the unstrained and strained FeN_3 sites.

3.3. Influence on NRR Selectivity. Furthermore, we examined the influence of structural distortion on the selectivity toward NRR on the FeN_4 and FeN_3 sites using the DFT calculation method. The competing HER is believed to be the most primary factor affecting the selectivity of the catalysts for NRR.[10,32,76,80] The free energy of H adsorption is proposed to be a descriptor to measure the HER activity.[31,73,81] Our DFT calculations predict that H would be adsorbed on top of the central Fe in the FeN_4 and FeN_3 sites as shown in Figure 6a,b. The free energy evolution for HER on the FeN_4 and FeN_3 sites (Figure 6a,b) indicates that the compressive strain would cause the free energy change of *H adsorption to be closer to 0 eV, which indicates that the competing HER is promoted by compressive strain at these active sites.[82] The values of calculated free energy change for the adsorption *H (ΔG_{*H}) on the unstrained and strained FeN_4 and FeN_3 sites are given in Table 2. ΔG_{*H} is predicted to decrease from 0.24 eV on the unstrained FeN_4 site to 0.16 eV on the strained one, while ΔG_{*H} only increases from −0.41 eV on the unstrained FeN_3 site to −0.38 eV on the strained one. It should be noted that our predicted free energy changes ΔG_{*H} for *H adsorption on the unstrained FeN_4 site (0.24 eV) and on the unstrained FeN_3 site (−0.41 eV) are consistent with previous predictions of 0.40 eV on FeN_4 and −0.53 eV on FeN_3.[42,69] We also performed the bonding analysis for the *H adsorption on FeN_4 and FeN_3 sites to understand the compressive strain effect on the HER activity. Most valence states (below E_F) of *H adsorption are bonding in nature on the strained and unstrained FeN_4 sites, while only a few antibonding states can be found at vicinity below the Fermi level (Figure 7a). The integrated pCOHP for the Fe−H bonding on the FeN_4 sites decreases from −1.21 eV on unstrained one to −1.25 eV on strained one, which suggests a stronger binding of *H adsorption on the strained FeN_4 sites. In contrast, antibonding states are only visible above the Fermi level for the Fe−H bonding on FeN_3 sites (Figure 7b). The −pCOHP curves of the strained and unstrained FeN_3 sites are almost identical in the valence bands, and the ICOHP on the strained FeN_3 site only increases less than 0.01 eV as compared to the one on the unstrained FeN_3 site, both implying a very similar binding strength of *H on FeN_3 sites with and without strain.

Regarding the NRR selectivity of catalysts, several computational methods have been employed in previous studies. For example, some researchers proposed to compare the adsorption energies of $*N_2$ and *H (i.e., $\Delta G_{*N_2} - \Delta G_{*H}$) on the same active site as a descriptor for measurement of the NRR selectivity.[31,34,69,73,76,83] If an active site can be preferably occupied by $*N_2$ over *H, the competing HER will be effectively suppressed. Hence, the active sites with a more negative value of $\Delta G_{*N2} - \Delta G_{*H}$ should exhibit better selectivity for NRR over HER. Our DFT results in Table 2 indicate that the compressively strained FeN_4 and FeN_3 sites would have a better selectivity toward NRR than the unstrained ones. Some studies used the free energy difference between *NNH and *H adsorption (i.e., $\Delta G_{*NNH} - \Delta G_{*H}$) to gauge the NRR selectivity,[84] because the hydrogenation step from $*N_2$ to *NNH is the PDS of NRR. Here, *NNH is the

Table 2. Calculated Free Energy Changes as Related to NRR Selectivity on FeN_4 and FeN_3 Sites

	FeN_4		FeN_3	
	unstrained	strained	unstrained	strained
ΔG_{*H} (eV)	0.24	0.16	−0.41	−0.38
$\Delta G_{*N_2} - \Delta G_{*H}$ (eV)	−0.30	−0.42	−0.45	−0.56
$\Delta G_{*NNH} - \Delta G_{*H}$ (eV)	1.01	0.68	0.37	0.25
$U_{L(NRR)} - U_{L(HER)}$ (V)	−1.07	−0.94	−1.24	−1.18

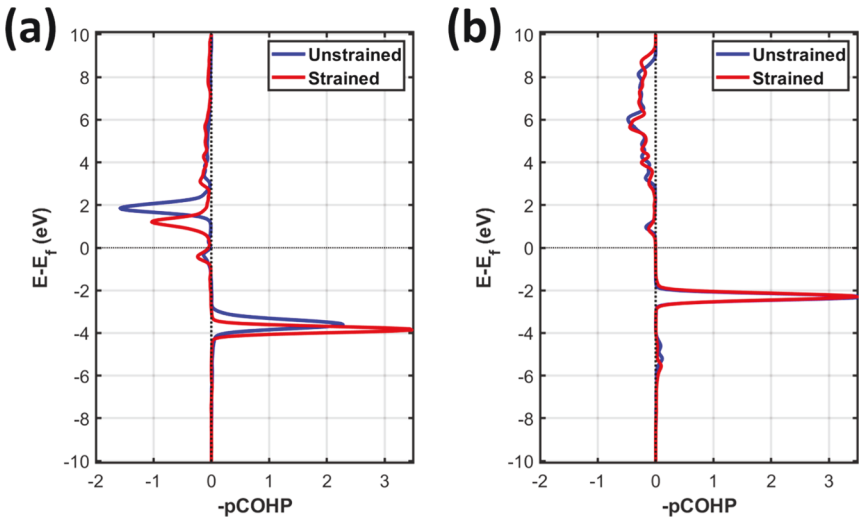

Figure 7. pCOHP analysis for the Fe−H bond between the central Fe and the adsorbed *H on (a) FeN_4 and (b) FeN_3 sites with and without strain.

https://doi.org/10.1021/acs.jpcc.1c04510
J. Phys. Chem. C 2021, 125, 16004−16012

preferred adsorbed species over *H for selective NRR. We predicted more negative values of $\Delta G_{*NNH} - \Delta G_{*H}$ on the compressively strained FeN_4 and FeN_3 sites shown in Table 2, and thus a better NRR selectivity on the strained sites than the unstrained ones. In addition, the limiting potential difference between NRR and HER ($U_{L(NRR)} - U_{L(HER)}$) was employed to describe the NRR selectivity.[79−81] For HER on the FeN_3 sites, which shows a negative free change of *H adsorption, the limiting potential here is defined as the largest electrode potential that can keep the process thermodynamically favorable. The negative value of limiting potential difference shown in Table 2 indicates the HER always have less negative limiting potential than NRR on both FeN_4 and FeN_3 sites, which implies the HER is indeed competitive with the NRR. However, our results show that the compressive strain on both FeN_4 and FeN_3 sites leads to a less negative limiting potential difference between the NRR and HER, which indicates a smaller activity difference between NRR and HER on the strained active sites. Thus, the NRR selectivity is enhanced on the compressively strained FeN_4 and FeN_3 sites.

For the calculated values from all the methods listed in Table 2, the strained FeN_4 sites have a more negative $\Delta G_{*N2} - \Delta G_{*H}$ by 0.12 eV, a more negative $\Delta G_{*NNH} - \Delta G_{*H}$ by 0.33 eV, and a less negative $U_{L(NRR)} - U_{L(HER)}$ by 0.13 V as compared to the unstrained FeN_4 sites, respectively. In contrast, the strained FeN_3 sites only have a more negative $\Delta G_{*N2} - \Delta G_{*H}$ by 0.11 eV, a more negative $\Delta G_{*NNH} - \Delta G_{*H}$ by 0.12 eV, and a less negative $U_{L(NRR)} - U_{L(HER)}$ by 0.06 V as compared to the unstrained FeN_3 sites. Therefore, we predict that the structural distortion due to compressive strain would have a more pronounced influence on the NRR selectivity on FeN_4 sites than on FeN_3 sites.

4. CONCLUSIONS

In this study, we have investigated the influence of structural distortion on the activity and selectivity of Fe−N−C catalysts for NRR using the first-principles DFT calculations. The structural distortion was induced through formation of curved graphene layers, as compared to planar layers, under compressive strain. Our computational results reveal that the structural distortion could change the NRR pathways from a hybrid path to a distal one on the compressively strained FeN_4 and FeN_3 sites. Using the calculated limiting potential for NRR as an indicator, we further predicted that the catalytic activity would be enhanced by a 0.21 V positive change in limiting potential on the strained FeN_4 site than that on the unstrained one, and by a 0.03 V positive change in limiting potential on the strained FeN_3 site than that on the unstrained one. Moreover, we employed three different computational quantities to demonstrate that the selectivity toward NRR over HER has also been enhanced by the compressive strain on both FeN_4 and FeN_3 sites. Therefore, our computational results indicate that the structural distortion induced by compressive strain in the graphene layer is beneficial for catalytic performance improvement in Fe−N−C catalysts for NRR. Thus, this study suggests an effective and novel concept for rational design and synthesis of metal and nitrogen codoped carbon as a high performance electrocatalyst for ammonia production.

■ AUTHOR INFORMATION

Corresponding Author

Guofeng Wang − *Department of Mechanical Engineering and Materials Science, University of Pittsburgh, Pittsburgh, Pennsylvania 15261, United States;* orcid.org/0000-0001-8249-4101; Email: guw8@pitt.edu

Author

Weitao Shan − *Department of Mechanical Engineering and Materials Science, University of Pittsburgh, Pittsburgh, Pennsylvania 15261, United States;* orcid.org/0000-0002-5414-5710

Complete contact information is available at: https://pubs.acs.org/10.1021/acs.jpcc.1c04510

Notes

The authors declare no competing financial interest.

■ ACKNOWLEDGMENTS

This work was supported by a research grant from U.S. National Science Foundation (NSF CBET #1804534). The authors also gratefully acknowledge the computational resources provided by the Center for Research Computing of the University of Pittsburgh and the Extreme Science and Engineering Discovery Environment (XSEDE).

■ REFERENCES

(1) Smil, V. Detonator of the population explosion. *Nature* **1999**, *400*, 415.

(2) Shipman, M. A.; Symes, M. D. Recent progress towards the electrosynthesis of ammonia from sustainable resources. *Catal. Today* **2017**, *286*, 57−68.

(3) Chen, G. F.; Ren, S.; Zhang, L.; Cheng, H.; Luo, Y.; Zhu, K.; Ding, L. X.; Wang, H. Advances in electrocatalytic N_2 reduction—strategies to tackle the selectivity challenge. *Small Methods* **2019**, *3*, 1800337.

(4) Chen, J. G.; Crooks, R. M.; Seefeldt, L. C.; Bren, K. L.; Bullock, R. M.; Darensbourg, M. Y.; Holland, P. L.; Hoffman, B.; Janik, M. J.; Jones, A. K.; et al. Beyond fossil fuel-driven nitrogen transformations. *Science* **2018**, *360*, No. eaar6611.

(5) Rafiqul, I.; Weber, C.; Lehmann, B.; Voss, A. Energy efficiency improvements in ammonia production—perspectives and uncertainties. *Energy* **2005**, *30*, 2487−2504.

(6) Schrock, R. R. Catalytic reduction of dinitrogen to ammonia at well-defined single metal sites. *Philos. Trans. R. Soc., A* **2005**, *363*, 959−969.

(7) Kitano, M.; Inoue, Y.; Yamazaki, Y.; Hayashi, F.; Kanbara, S.; Matsuishi, S.; Yokoyama, T.; Kim, S.-W.; Hara, M.; Hosono, H. Ammonia synthesis using a stable electride as an electron donor and reversible hydrogen store. *Nat. Chem.* **2012**, *4*, 934.

(8) Song, P.; Wang, H.; Kang, L.; Ran, B.; Song, H.; Wang, R. Electrochemical nitrogen reduction to ammonia at ambient conditions on nitrogen and phosphorus co-doped porous carbon. *Chem. Commun.* **2019**, *55*, 687−690.

(9) Van der Ham, C. J. M.; Koper, M. T. M.; Hetterscheid, D. G. H. Challenges in reduction of dinitrogen by proton and electron transfer. *Chem. Soc. Rev.* **2014**, *43*, 5183−5191.

(10) Singh, A. R.; Rohr, B. A.; Schwalbe, J. A.; Cargnello, M.; Chan, K.; Jaramillo, T. F.; Chorkendorff, I.; Nørskov, J. K. Electrochemical Ammonia Synthesis-The Selectivity Challenge. *ACS Catal.* **2017**, *7*, 706−709.

(11) Cui, X.; Tang, C.; Zhang, Q. A review of electrocatalytic reduction of dinitrogen to ammonia under ambient conditions. *Adv. Energy Mater.* **2018**, *8*, 1800369.

(12) Guo, C.; Ran, J.; Vasileff, A.; Qiao, S.-Z. Rational design of electrocatalysts and photo (electro) catalysts for nitrogen reduction to

ammonia (NH_3) under ambient conditions. *Energy Environ. Sci.* **2018**, *11*, 45−56.
(13) Diekhöner, L.; Mortensen, H.; Baurichter, A.; Luntz, A. C. Laser assisted associative desorption of N_2 and CO from Ru (0001). *J. Chem. Phys.* **2001**, *115*, 3356−3373.
(14) Rod, T. H.; Logadottir, A.; Nørskov, J. K. Ammonia synthesis at low temperatures. *J. Chem. Phys.* **2000**, *112*, 5343−5347.
(15) Kordali, V.; Kyriacou, G.; Lambrou, C. Electrochemical synthesis of ammonia at atmospheric pressure and low temperature in a solid polymer electrolyte cell. *Chem. Commun.* **2000**, *17*, 1673−1674.
(16) Lan, R.; Irvine, J. T. S.; Tao, S. Synthesis of ammonia directly from air and water at ambient temperature and pressure. *Sci. Rep.* **2013**, *3*, 1145.
(17) Lan, R.; Tao, S. Electrochemical synthesis of ammonia directly from air and water using a $Li^+/H^+/NH_4^+$ mixed conducting electrolyte. *RSC Adv.* **2013**, *3*, 18016−18021.
(18) Bao, D.; Zhang, Q.; Meng, F.-L.; Zhong, H.-X.; Shi, M.-M.; Zhang, Y.; Yan, J.-M.; Jiang, Q.; Zhang, X.-B. Electrochemical reduction of N_2 under ambient conditions for artificial N_2 fixation and renewable energy storage using N_2/NH_3 cycle. *Adv. Mater.* **2017**, *29*, 1604799.
(19) Li, S.-J.; Bao, D.; Shi, M.-M.; Wulan, B.-R.; Yan, J.-M.; Jiang, Q. Amorphizing of Au nanoparticles by CeOx−RGO hybrid support towards highly efficient electrocatalyst for N_2 reduction under ambient conditions. *Adv. Mater.* **2017**, *29*, 1700001.
(20) Shi, M.-M.; Bao, D.; Wulan, B.-R.; Li, Y.-H.; Zhang, Y.-F.; Yan, J.-M.; Jiang, Q. Au sub-nanoclusters on TiO_2 toward highly efficient and selective electrocatalyst for N_2 conversion to NH_3 at ambient conditions. *Adv. Mater.* **2017**, *29*, 1606550.
(21) Kim, K.; Lee, N.; Yoo, C.-Y.; Kim, J.-N.; Yoon, H. C.; Han, J.-I. Communication—electrochemical reduction of nitrogen to ammonia in 2-propanol under ambient temperature and pressure. *J. Electrochem. Soc.* **2016**, *163*, F610−F612.
(22) Kim, K.; Yoo, C.-Y.; Kim, J.-N.; Yoon, H. C.; Han, J.-I. Electrochemical synthesis of ammonia from water and nitrogen in ethylenediamine under ambient temperature and pressure. *J. Electrochem. Soc.* **2016**, *163*, F1523−F1526.
(23) Yang, D.; Chen, T.; Wang, Z. Electrochemical reduction of aqueous nitrogen (N_2) at a low overpotential on (110)-oriented Mo nanofilm. *J. Mater. Chem. A* **2017**, *5*, 18967−18971.
(24) Skúlason, E.; Bligaard, T.; Gudmundsdóttir, S.; Studt, F.; Rossmeisl, J.; Abild-Pedersen, F.; Vegge, T.; Jónsson, H.; Nørskov, J. K. A theoretical evaluation of possible transition metal electrocatalysts for N_2 reduction. *Phys. Chem. Chem. Phys.* **2012**, *14*, 1235−1245.
(25) Foster, S. L.; Bakovic, S. I. P.; Duda, R. D.; Maheshwari, S.; Milton, R. D.; Minteer, S. D.; Janik, M. J.; Renner, J. N.; Greenlee, L. F. Catalysts for nitrogen reduction to ammonia. *Nat. Catal.* **2018**, *1*, 490−500.
(26) Furuya, N.; Yoshiba, H. Electroreduction of nitrogen to ammonia on gas-diffusion electrodes loaded with inorganic catalyst. *J. Electroanal. Chem. Interfacial Electrochem.* **1990**, *291*, 269−272.
(27) Zhang, R.; Ren, X.; Shi, X.; Xie, F.; Zheng, B.; Guo, X.; Sun, X. Enabling effective electrocatalytic N_2 conversion to NH_3 by the TiO_2 nanosheets array under ambient conditions. *ACS Appl. Mater. Interfaces* **2018**, *10*, 28251−28255.
(28) Li, Y.-b.; Liu, Y.-p.; Wang, J.; Guo, Y.-l.; Chu, K. Plasma-engineered NiO nanosheets with enriched oxygen vacancies for enhanced electrocatalytic nitrogen fixation. *Inorg. Chem. Front.* **2020**, *7*, 455−463.
(29) Zhang, L.; Ji, X.; Ren, X.; Ma, Y.; Shi, X.; Tian, Z.; Asiri, A. M.; Chen, L.; Tang, B.; Sun, X. Electrochemical ammonia synthesis via nitrogen reduction reaction on a MoS_2 catalyst: theoretical and experimental studies. *Adv. Mater.* **2018**, *30*, 1800191.
(30) Le, Y.-Q.; Gu, J.; Tian, W. Q. Nitrogen-fixation catalyst based on graphene: every part counts. *Chem. Commun.* **2014**, *50*, 13319−13322.
(31) Choi, C.; Back, S.; Kim, N.-Y.; Lim, J.; Kim, Y.-H.; Jung, Y. Suppression of Hydrogen Evolution Reaction in Electrochemical N_2 Reduction Using Single-Atom Catalysts: A Computational Guideline. *ACS Catal.* **2018**, *8*, 7517−7525.
(32) Mukherjee, S.; Yang, X.; Shan, W.; Samarakoon, W.; Karakalos, S.; Cullen, D. A.; More, K.; Wang, M.; Feng, Z.; Wang, G.; et al. Atomically dispersed single Ni site catalysts for nitrogen reduction toward electrochemical ammonia synthesis using N_2 and H_2O. *Small Methods* **2020**, *4*, 1900821.
(33) Geng, Z.; Liu, Y.; Kong, X.; Li, P.; Li, K.; Liu, Z.; Du, J.; Shu, M.; Si, R.; Zeng, J. Achieving a Record-High Yield Rate of 120.9 for N_2 Electrochemical Reduction over Ru Single-Atom Catalysts. *Adv. Mater.* **2018**, *30*, 1803498.
(34) Tao, H.; Choi, C.; Ding, L.-X.; Jiang, Z.; Han, Z.; Jia, M.; Fan, Q.; Gao, Y.; Wang, H.; Robertson, A. W.; et al. Nitrogen fixation by Ru single-atom electrocatalytic reduction. *Chem* **2019**, *5*, 204−214.
(35) Lancaster, K. M.; Roemelt, M.; Ettenhuber, P.; Hu, Y.; Ribbe, M. W.; Neese, F.; Bergmann, U.; DeBeer, S. X-ray emission spectroscopy evidences a central carbon in the nitrogenase iron-molybdenum cofactor. *Science* **2011**, *334*, 974−977.
(36) Spatzal, T.; Aksoyoglu, M.; Zhang, L.; Andrade, S. L. A.; Schleicher, E.; Weber, S.; Rees, D. C.; Einsle, O. Evidence for interstitial carbon in nitrogenase FeMo cofactor. *Science* **2011**, *334*, 940.
(37) Furuya, N.; Yoshiba, H. Electroreduction of nitrogen to ammonia on gas-diffusion electrodes modified by Fe-phthalocyanine. *J. Electroanal. Chem. Interfacial Electrochem.* **1989**, *263*, 171−174.
(38) Zhao, X.; Yin, F.; Liu, N.; Li, G.; Fan, T.; Chen, B. Highly efficient metal−organic-framework catalysts for electrochemical synthesis of ammonia from N_2 (air) and water at low temperature and ambient pressure. *J. Mater. Sci.* **2017**, *52*, 10175−10185.
(39) Yang, X.; Sun, S.; Meng, L.; Li, K.; Mukherjee, S.; Chen, X.; Lv, J.; Liang, S.; Zang, H.-Y.; Yan, L.-K.; et al. Molecular single iron site catalysts for electrochemical nitrogen fixation under ambient conditions. *Appl. Catal., B* **2021**, *285*, 119794.
(40) Cong, M.; Chen, X.; Xia, K.; Ding, X.; Zhang, L.; Jin, Y.; Gao, Y.; Zhang, L. Selective nitrogen reduction to ammonia on iron porphyrin-based single-site metal−organic frameworks. *J. Mater. Chem. A* **2021**, *9*, 4673−4678.
(41) Li, Y.; Li, J.; Huang, J.; Chen, J.; Kong, Y.; Yang, B.; Li, Z.; Lei, L.; Chai, G.; Wen, Z.; et al. Boosting Electroreduction Kinetics of Nitrogen to Ammonia via Tuning Electron Distribution of Single-Atomic Iron Sites. *Angew. Chem., Int. Ed.* **2021**, *60*, 9078−9085.
(42) Wang, Y.; Cui, X.; Zhao, J.; Jia, G.; Gu, L.; Zhang, Q.; Meng, L.; Shi, Z.; Zheng, L.; Wang, C.; et al. Rational Design of Fe−N/C Hybrid for Enhanced Nitrogen Reduction Electrocatalysis under Ambient Conditions in Aqueous Solution. *ACS Catal.* **2019**, *9*, 336−344.
(43) Lü, F.; Zhao, S.; Guo, R.; He, J.; Peng, X.; Bao, H.; Fu, J.; Han, L.; Qi, G.; Luo, J.; et al. Nitrogen-coordinated single Fe sites for efficient electrocatalytic N_2 fixation in neutral media. *Nano Energy* **2019**, *61*, 420−427.
(44) Mounet, N.; Marzari, N. First-principles determination of the structural, vibrational and thermodynamic properties of diamond, graphite, and derivatives. *Phys. Rev. B: Condens. Matter Mater. Phys.* **2005**, *71*, 205214.
(45) Bao, W.; Miao, F.; Chen, Z.; Zhang, H.; Jang, W.; Dames, C.; Lau, C. N. Controlled ripple texturing of suspended graphene and ultrathin graphite membranes. *Nat. Nanotechnol.* **2009**, *4*, 562.
(46) Pozzo, M.; Alfè, D.; Lacovig, P.; Hofmann, P.; Lizzit, S.; Baraldi, A. Thermal expansion of supported and freestanding graphene: lattice constant versus interatomic distance. *Phys. Rev. Lett.* **2011**, *106*, 135501.
(47) Yoon, D.; Son, Y.-W.; Cheong, H. Negative thermal expansion coefficient of graphene measured by Raman spectroscopy. *Nano Lett.* **2011**, *11*, 3227−3231.
(48) Li, J.; Zhang, H.; Samarakoon, W.; Shan, W.; Cullen, D. A.; Karakalos, S.; Chen, M.; Gu, D.; More, K. L.; Wang, G.; et al. Thermally driven structure and performance evolution of atomically

dispersed FeN_4 sites for oxygen reduction. *Angew. Chem., Int. Ed.* **2019**, *58*, 18971−18980.
(49) Mohd Adli, N.; Shan, W.; Hwang, S.; Samarakoon, W.; Karakalos, S.; Li, Y.; Cullen, D. A.; Su, D.; Feng, Z.; Wang, G.; et al. Engineering Atomically Dispersed FeN_4 Active Sites for CO_2 Electroreduction. *Angew. Chem., Int. Ed.* **2021**, *133*, 1035−1045.
(50) Hohenberg, P.; Kohn, W. Inhomogeneous electron gas. *Phys. Rev.* **1964**, *136*, B864−B871.
(51) Kohn, W.; Sham, L. J. Self-consistent equations including exchange and correlation effects. *Phys. Rev.* **1965**, *140*, A1133−A1138.
(52) Parr, R. G.; Yang, W. *Density-functional theory of atoms and molecules*; Oxford university press, 1989; Vol. *16*.
(53) Kresse, G.; Hafner, J. Ab initio molecular-dynamics simulation of the liquid-metal−amorphous-semiconductor transition in germanium. *Phys. Rev. B* **1994**, *49*, 14251.
(54) Kresse, G.; Furthmüller, J. Efficient iterative schemes for ab initio total-energy calculations using a plane-wave basis set. *Phys. Rev. B* **1996**, *54*, 11169.
(55) Kresse, G.; Furthmüller, J. Efficiency of ab-initio total energy calculations for metals and semiconductors using a plane-wave basis set. *Comput. Mater. Sci.* **1996**, *6*, 15−50.
(56) Kresse, G.; Joubert, D. From ultrasoft pseudopotentials to the projector augmented-wave method. *Phys. Rev. B* **1999**, *59*, 1758.
(57) Blöchl, P. E. Projector augmented-wave method. *Phys. Rev. B* **1994**, *50*, 17953.
(58) Perdew, J. P.; Burke, K.; Ernzerhof, M. Generalized gradient approximation made simple. *Phys. Rev. Lett.* **1996**, *77*, 3865.
(59) Perdew, J. P.; Chevary, J. A.; Vosko, S. H.; Jackson, K. A.; Pederson, M. R.; Singh, D. J.; Fiolhais, C. Atoms, molecules, solids, and surfaces: Applications of the generalized gradient approximation for exchange and correlation. *Phys. Rev. B* **1992**, *46*, 6671.
(60) Tkatchenko, A.; Scheffler, M. Accurate molecular van der Waals interactions from ground-state electron density and free-atom reference data. *Phys. Rev. Lett.* **2009**, *102*, 073005.
(61) Bučko, T.; Lebègue, S.; Hafner, J.; Angyan, J. G. Tkatchenko-Scheffler van der Waals correction method with and without self-consistent screening applied to solids. *Phys. Rev. B: Condens. Matter Mater. Phys.* **2013**, *87*, 064110.
(62) Monkhorst, H. J.; Pack, J. D. Special points for Brillouin-zone integrations. *Phys. Rev. B: Solid State* **1976**, *13*, 5188.
(63) Nørskov, J. K.; Rossmeisl, J.; Logadottir, A.; Lindqvist, L.; Kitchin, J. R.; Bligaard, T.; Jonsson, H. Origin of the overpotential for oxygen reduction at a fuel-cell cathode. *J. Phys. Chem. B* **2004**, *108*, 17886−17892.
(64) Allison, T. *JANAF Thermochemical Tables, NIST Standard Reference Database 13*; National Institute of Standards and Technology, 1996.
(65) Dronskowski, R.; Bloechl, P. E. Crystal orbital Hamilton populations (COHP): energy-resolved visualization of chemical bonding in solids based on density-functional calculations. *J. Phys. Chem.* **1993**, *97*, 8617−8624.
(66) Deringer, V. L.; Tchougréeff, A. L.; Dronskowski, R. Crystal orbital Hamilton population (COHP) analysis as projected from plane-wave basis sets. *J. Phys. Chem. A* **2011**, *115*, 5461−5466.
(67) Nelson, R.; Ertural, C.; George, J.; Deringer, V. L.; Hautier, G.; Dronskowski, R. LOBSTER: Local orbital projections, atomic charges, and chemical-bonding analysis from projector-augmented-wave-based density-functional theory. *J. Comput. Chem.* **2020**, *41*, 1931−1940.
(68) Maintz, S.; Deringer, V. L.; Tchougréeff, A. L.; Dronskowski, R. LOBSTER: A tool to extract chemical bonding from plane-wave based DFT. *J. Comput. Chem.* **2016**, *37*, 1030−1035.
(69) Yang, Y.; Liu, J.; Wei, Z.; Wang, S.; Ma, J. Transition metal-dinitrogen complex embedded graphene for nitrogen reduction reaction. *ChemCatChem* **2019**, *11*, 2821−2827.
(70) Li, X.-F.; Li, Q.-K.; Cheng, J.; Liu, L.; Yan, Q.; Wu, Y.; Zhang, X.-H.; Wang, Z.-Y.; Qiu, Q.; Luo, Y. Conversion of dinitrogen to ammonia by FeN_3-embedded graphene. *J. Am. Chem. Soc.* **2016**, *138*, 8706−8709.
(71) Hinnemann, B.; Nørskov, J. K. Chemical activity of the nitrogenase FeMo cofactor with a central nitrogen ligand: density functional study. *J. Am. Chem. Soc.* **2004**, *126*, 3920−3927.
(72) Barney, B. M.; Lukoyanov, D.; Yang, T.-C.; Dean, D. R.; Hoffman, B. M.; Seefeldt, L. C. A methyldiazene ($HN{=}N{-}CH_3$)-derived species bound to the nitrogenase active-site FeMo cofactor: Implications for mechanism. *Proc. Natl. Acad. Sci. U.S.A.* **2006**, *103*, 17113−17118.
(73) Ling, C.; Ouyang, Y.; Li, Q.; Bai, X.; Mao, X.; Du, A.; Wang, J. A General two-step strategy−based high-throughput screening of single atom catalysts for nitrogen fixation. *Small Methods* **2019**, *3*, 1800376.
(74) Liu, X.; Jiao, Y.; Zheng, Y.; Jaroniec, M.; Qiao, S.-Z. Building up a picture of the electrocatalytic nitrogen reduction activity of transition metal single-atom catalysts. *J. Am. Chem. Soc.* **2019**, *141*, 9664−9672.
(75) Ma, Z.; Cui, Z.; Xiao, C.; Dai, W.; Lv, Y.; Li, Q.; Sa, R. Theoretical screening of efficient single-atom catalysts for nitrogen fixation based on a defective BN monolayer. *Nanoscale* **2020**, *12*, 1541−1550.
(76) Guo, Y.; Wang, G.; Shen, S.; Wei, G.; Xia, G.; Zhang, J. On scaling relations of single atom catalysts for electrochemical ammonia synthesis. *Appl. Surf. Sci.* **2021**, *550*, 149283.
(77) Maintz, S.; Deringer, V. L.; Tchougréeff, A. L.; Dronskowski, R. Analytic projection from plane-wave and PAW wavefunctions and application to chemical-bonding analysis in solids. *J. Comput. Chem.* **2013**, *34*, 2557−2567.
(78) Hao, Y.-C.; Guo, Y.; Chen, L.-W.; Shu, M.; Wang, X.-Y.; Bu, T.-A.; Gao, W.-Y.; Zhang, N.; Su, X.; Feng, X.; et al. Promoting nitrogen electroreduction to ammonia with bismuth nanocrystals and potassium cations in water. *Nat. Catal.* **2019**, *2*, 448−456.
(79) Guo, X.; Gu, J.; Hu, X.; Zhang, S.; Chen, Z.; Huang, S. Coordination tailoring towards efficient single-atom catalysts for N_2 fixation: A case study of iron-nitrogen-carbon (Fe@N-C) systems. *Catal. Today* **2020**, *350*, 91−99.
(80) Singh, A. R.; Rohr, B. A.; Statt, M. J.; Schwalbe, J. A.; Cargnello, M.; Nørskov, J. K. Strategies toward selective electrochemical ammonia synthesis. *ACS Catal.* **2019**, *9*, 8316−8324.
(81) Montoya, J. H.; Tsai, C.; Vojvodic, A.; Nørskov, J. K. The challenge of electrochemical ammonia synthesis: A new perspective on the role of nitrogen scaling relations. *ChemSusChem* **2015**, *8*, 2180−2186.
(82) Liu, C.; Li, Q.; Wu, C.; Zhang, J.; Jin, Y.; MacFarlane, D. R.; Sun, C. Single-boron catalysts for nitrogen reduction reaction. *J. Am. Chem. Soc.* **2019**, *141*, 2884−2888.
(83) Li, Q.; He, L.; Sun, C.; Zhang, X. Computational study of MoN_2 monolayer as electrochemical catalysts for nitrogen reduction. *J. Phys. Chem. C* **2017**, *121*, 27563−27568.
(84) Zhao, W.; Zhang, L.; Luo, Q.; Hu, Z.; Zhang, W.; Smith, S.; Yang, J. Single $Mo_1(Cr_1)$ Atom on Nitrogen-Doped Graphene Enables Highly Selective Electroreduction of Nitrogen into Ammonia. *ACS Catal.* **2019**, *9*, 3419−3425.

https://doi.org/10.1021/acs.jpcc.1c04510
J. Phys. Chem. C 2021, 125, 16004−16012